Science Bulletin 65 (2020) 1650–1658

Contents lists available at ScienceDirect

Science Bulletin

journal homepage: www.elsevier.com/locate/scib

Article

Adjustment of oxygen vacancy states in ZnO and its application in ppb-level NO_2 gas sensor

Gaoda Li [1], Heng Zhang [1], Leixin Meng, Zhe Sun, Zhao Chen, Xiaoyu Huang, Yong Qin *

Institute of Nanoscience and Nanotechnology, School of Physical Science and Technology, Lanzhou University, Lanzhou 730000, China

ARTICLE INFO

Article history:
Received 26 March 2020
Received in revised form 6 May 2020
Accepted 20 May 2020
Available online 28 May 2020

Keywords:
Gas sensor
Sensing mechanism
Oxygen vacancy states
Adsorption

ABSTRACT

Oxygen vacancy (V_O) is long believed as a key factor influencing the gas sensing properties. However, the concentration of V_O is generally focused while the V_O state is neglected, which masks the inherent mechanism of gas sensor. Using a post annealing process, the influence of V_O states on the response of ZnO nanofilm to NO_2 gas is investigated in this study. The systematical analysis of the results obtained by different methods indicates a transformation of V_O from the neutral to the doubly ionized state during post annealing treatment. The results also imply that the gas sensing properties is not directly correlated with the V_O concentration. And due to the competitive adsorption of ambient O_2, the neutral V_O is majorly occupied by the adsorbed O_2 while the V_O in doubly ionized state can promote the adsorption of NO_2. Consequently, the transition of V_O from the neutral to the doubly ionized state can lead to a dramatic increase of the response to NO_2, from 733 to 3.34×10^4 for 100 ppm NO_2. Guided by this mechanism, NO_2 gas sensing in ppb-level is also achieved: the response reaches 165% to 25 ppb (0.025 ppm) NO_2 with a good repeatability.

1. Introduction

In recent years, ppb-level gas sensors are highly desirable due to its importance in the monitoring of indoor/outdoor air condition [1,2], the industrial workplace monitoring [3], and the diagnose of specific diseases [4,5]. To achieve the ppb-level detection, oxygen vacancy (V_O) is believed as a key factor and enormous effort is put to examine the influence of V_O on the gas sensing properties [6–17]. Different methods have been used to adjust the concentration of V_O: doping with different elements [18–22], post-annealing in different atmospheres [8,11,23–25], slow cooling [26–28], and morphology control for example [7,10]. It is believed that the increase of V_O concentration in sensing materials can enhance the adsorption of target gas and result to the increase of gas sensitivity.

For oxidizing gas, NO_2 for example, its binding energy on oxygen vacancy would be larger than that on perfect surface [1,2,7,29–31]. Consequently, the increase of V_O concentration would result to the enhanced adsorption of NO_2. For reducing gas, its reaction with ionized oxygen species formed during the adsorption of ambient oxygen would be enhanced due to the enhanced adsorption of O_2 on V_O [10,32,33]. However, a problem is caused naturally in above explanations: as oxidizing gases, NO_2 and ambient O_2 would compete with each other to build an equilibrium between surface adsorbents, surface adsorbing sites, and free electrons in sensing materials [34]. Correlated with the transfer of electrons from sensing materials to adsorbents, the adsorption of NO_2 and ambient O_2 would both be enhanced by surface V_O while limited by the available adsorption sites, free electron concentration and surface band bending. With only the V_O concentration taken into consideration, the underlying mechanism cannot be fully explained and the advantage of V_O to the gas sensing is not fully realized as a result. To resolve this problem, the influence of V_O states should be taken into consideration, and the gas adsorption on V_O in different states should be compared.

As a widely used and typical gas sensing material, ZnO is used in this work to investigate the influence of the V_O states on its NO_2 sensing properties. There are three different V_O states in ZnO: neutral vacancy V_O^0 (V_O^X in Kröger-Vink notation), singly ionized vacancy V_O^{1+} ($V_O^{\cdot}$), and ionized 2+ state V_O^{2+} ($V_O^{\cdot\cdot}$). They have different defect formation energies and electron states, which would result to the complex photoluminescence and electronic properties [35–38]. The relative V_O concentration can be obtained using X-ray photoelectron spectroscopy (XPS) [2], while the ratios of V_O in different states cannot be obtained directly. V_O^{1+} can be characterized by electron paramagnetic resonance (EPR), while the

* Corresponding author.
E-mail address: qinyong@lzu.edu.cn (Y. Qin).
[1] These authors contributed equally to this work.

https://doi.org/10.1016/j.scib.2020.05.027
2095-9273/

experimental methods for V_O^0 and V_O^{2+} are limited. To some extends, photoluminescence (PL) can reveal the relative concentration of V_O in different states, but due to the complex defect structure of ZnO, the sources of different emissions are still in controversy [1,30,39,40].

To characterize V_O in different states and understand its influence on gas sensing, the results of XPS, EPR, PL, conductivity curves, and first principle calculation are compared and analyzed systematically in this work. It is found that the post-annealing treatment (200 to 400 °C) would result to a transformation of V_O from the neutral to the doubly ionized state, and this transformation would be reversed with the increase of annealing temperature or duration. The relative V_O concentration fluctuates, surface roughness and grain size of ZnO remain almost unchanged after the annealing process (200 to 450 °C). Furthermore, the adsorption of NO_2 is stronger than that of O_2 on V_O^{2+}, while a reversed relationship appears on V_O^0. Consequently, V_O^{2+} is much more efficient than V_O^0 and acts as the major factor in the enhancement of NO_2 sensing when ambient O_2 is present. Guided by this new found inner mechanism, the V_O^0 is transformed into V_O^{2+} in ZnO nanofilm under optimal annealing conditions, and the response to NO_2 gas sensor is enhanced dramatically by 45.6 times and reaches 3.34×10^4 to 100 ppm NO_2. Furthermore, NO_2 gas sensing in ppb-level is realized, which exhibits 165% response to 25 ppb NO_2 and a good repeatability.

2. Experimental

2.1. ZnO nanofilm and gas sensor

ZnO nanofilm was synthesized by the aqueous ink method [41]. NaOH (50 mL, 2.5 mol/L) aqueous solutions and $Zn(NO_3)_2$ aqueous solutions (75 mL, 0.5 mol/L) were mixed slowly under vigorously stirring. Hydrated precipitate was obtained after centrifugation and was dissolved in ammonia (250 mL, 6.6 mol/L) to form the Aqueous $Zn(OH)_x(NH_3)_y^{(2-x)+}$ solution. This precursor solution was dropped on a 1.6 cm × 1.6 cm quartz glass substrate, and spin coated at 1500 r/min for 1 min. The solution on substrate was dried at 100 °C, and annealed in furnace at different temperatures. In/Ag electrodes with 300 μm distance were sputtered on the top of quartz glass substrate by magnetron sputtering (100 W, 3 min for In, and 2 min for Ag).

2.2. Measurements

XPS measurements were conducted by a Kratos axis ultra delay-line detector (DLD) surface analysis instrument. EPR spectra were measured by a JES-FA300 instrument operating in X band frequency at room temperature. PL spectra were measured by a luminescence spectroscopy (FLS920T) with a 300 nm He-Cd laser as excitation source. The current was measured by an electrometer (B2985A) and voltage was applied by a function generator (DS345). The surface topography was measured by an atomic force microscopy (AFM, Bruker Dimension Icon). X-ray diffraction (XRD) measurement was conducted using grazing incidence diffraction mode (Panalytical X'Pert pro, Cu-Kα radiation) with a step size of 0.03° and from 20° to 90°. The gas sensing properties were measured by a home-made gas sensing system. Mixed gas composed of 20.9% O_2 and 79.1% N_2 by volume was used to simulate the dry air. During the test, the gas sensor was illuminated by UV light with 365 nm wavelength and 25 $\mu W/cm^2$ intensity to increase its response to NO_2 gas [34]. To realize ppb-level NO_2 gas, the flow rates of a standard 5 ppm NO_2 gas source (mixed with N_2) and a simulated dry air were controlled by two mass flow controllers.

2.3. Density functional theory (DFT) calculation

First principle calculation is used to calculate the defect formation energy, band structure and binding energy. Geometric optimizations were performed employing density functional theory [42–45]. Generalized gradient approximation (GGA) in the scheme of Perdew-Burke-Ernzerhof (PBE) was used to describe the exchange–correlation [46]. For ZnO bulk, a 3 × 2 × 2 supercell consisting of 24 ZnO formula, 380 eV plane-wave cutoff, and 2 × 2 × 1 Monkhorst-Pack sampling were used, and the system was fully relaxed until the final force was less than 0.01 eV/Å on each atom. To calculate the band structure, DFT + U approach was used [47,48]. The Hubbard U values are: Ud, Zn = 10.5 eV and Up, O = 7.0 eV. ZnO surfaces were modelled by period slabs using a 3 × 2 supercell (2 × 2 supercell for ZnO surfaces without vacancy) with 6 ZnO atomic layers and vacuum space of 15 Å. The bottom layer was fixed and other layers were relaxed. The NO_2 and O_2 molecules were firstly optimized in a (15 × 15 × 15) $Å^3$ sized cell. 340 eV energy cutoff, 2 × 2 × 1 Monkhorst-Pack k points sampling were used, and the system was fully relaxed until the final force was less than 0.03 eV/Å on each atom.

3. Results and discussion

3.1. Characterization of oxygen vacancies

The formation energy of defect D in charge state q can be calculated by [35]

$$\Delta H_{D,q}(E_f, \mu) = (E_{D,q} - E_H) + (\mu_X^{elem} + \Delta\mu_X) + q(E_V + \Delta E_f), \quad (1)$$

where $E_{D,q}$ is the total energy of the semiconductor with the defect D in charge state q, E_H is the energy of the perfect semiconductor, the second term describes the chemical potential of the removed anion X, and the third term refers to the energy of q electrons with respect to the valence band maximum. In ZnO and oxygen poor condition, the formation energies of oxygen vacancies in different charge states are calculated as a function of the Fermi level, as shown in Fig. 1. The valence band maximum (E_{VBM}) is set as zero. The formation energy of V_O^0 is 1.0 eV and generally larger than that of V_O^{2+}, until the Fermi level surpasses the thermal transition energy $\varepsilon(2+/0)$ (0.5 eV below the conduction band maximum, E_{CBM}). V_O^{1+} is generally unstable due to its formation energy in between, i.e., the negative-U character [36,37]. Due to the difference in formation energy, the transition of oxygen vacancy between different states, especially that between V_O^0 and V_O^{2+} is possible: V_O^0 can transform to V_O^{2+} thermally, and the transformation would be reversed when the Fermi level is larger than the thermal transition energy.

To reveal the relative concentration of V_O in ZnO and the influence of the post annealing process on the concentration, XPS characterization is conducted. It is known that the O 1s photoelectron peak is composed of three parts, as the fitting results shown in Fig. S1 (online): peak around 530.1, 531.1 and 532.2 eV, which are assigned to lattice oxygen O^{2-} (O^{2-} peak), oxygen atoms in vicinity of V_O (V_O peak), and oxygen from surface adsorbed oxygen species or hydroxyl groups (O_{ad} peak) respectively [2,23,39,49]. Due to the different annealing temperature, the relative intensity of different O 1s peaks varies and can be obtained by the integral-area ratios of V_O peak to O^{2-} peak or O 1s peak, as shown in Fig. 2a. With the increase of the annealing temperature, the ratio of V_O peak to O^{2-} peak increases until it reaches 300 °C. The highest ratio is 0.87 when the temperature reaches 300 or 400 °C. As to the ratio between V_O peak and O 1s peak, it fluctuates with the variation of annealing temperature due to the uncertainty in the area of O_{ad}. Compared with the relationship between ZnO nanofilm's

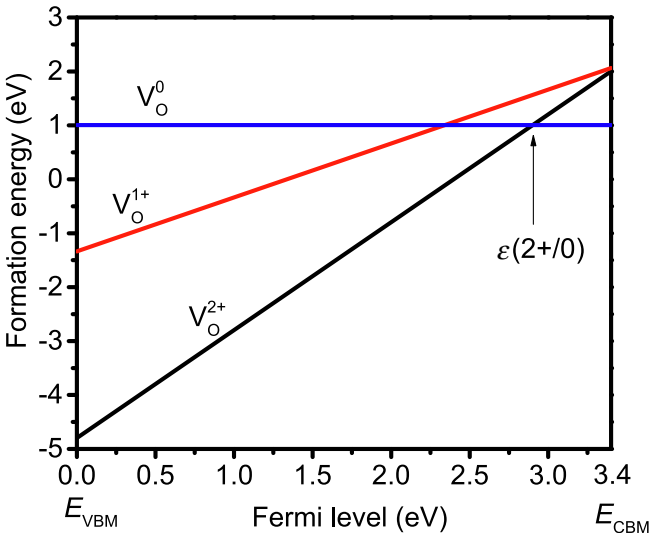

Fig. 1. (Color online) Relationship between the formation energy of oxygen vacancy in different states and the Fermi level.

response to NO_2 gas and the annealing temperature reported afterwards, no direct correlation can be found between the V_O concentration and the gas sensing properties due to their obvious different trends, as revealed afterwards.

The relative concentration of specific oxygen vacancy states cannot be directly obtained experimentally except that of V_O^{1+}, which can be characterized by EPR. The peak position in EPR spectra that associated with V_O^{1+} is still controversial, as connections with $g \sim 1.990$, 1.960, 1.996 and 2.003 are reported [24,40,50–53], and its relative intensity can be used to indicate the relative concentration of V_O^{1+} [50]. In our experiments, no obvious peak is observed in all samples as shown in Fig. 2b. This indicates that the V_O^{1+} concentration in ZnO annealed in different temperatures is quite low, and its influence on the gas sensing can be neglected. Furthermore, the conductivities of ZnO films fabricated under a same condition except for the annealing temperatures exhibit a turning point at 400 °C both in the dark (Fig. 2c) and under UV light (Fig. 2d).

The comparison between the relative concentration of V_O (Fig. 2a) and conductivities of ZnO nanofilms annealed in different temperatures (Fig. 2c, d) indicates that this turning point is not caused by the change of V_O concentration during annealing. The annealing process below 450 °C also has no influence on the crystal structure, grain size or surface morphology of ZnO nanofilms, as the XRD spectra and AFM characterization indicate. From the XRD spectra (Fig. S2 online), the crystallite sizes of ZnO nanofilms and lattice strain within are calculated by the Scherrer equation [54] (Table S1 online) and Williamson-Hall plots [55] (Fig. S3 and Table S2 online). Diameters of ZnO particles and surface roughness are also measured by AFM (Fig. S4 online). The results indicate that the annealing temperature below 450 °C has a little influence on the crystallite sizes, and the influence of roughness, crystallite size or lattice strain on conductivity can be eliminated. As revealed afterwards, the conductivity is correlated with the concentrations of V_O and V_O^{2+}.

As a relative indirect method, PL can be used to characterize V_O in ZnO [1,30,39,40]. However, due to the complex defect structure in ZnO, various sources are proposed to explain the PL spectra, especially the visible emission of ZnO: shallow donor, oxygen vacancy with different states, zinc vacancy, or oxygen and zinc interstitials [1,30,39,40,56–58]. To pinpoint the origin of different

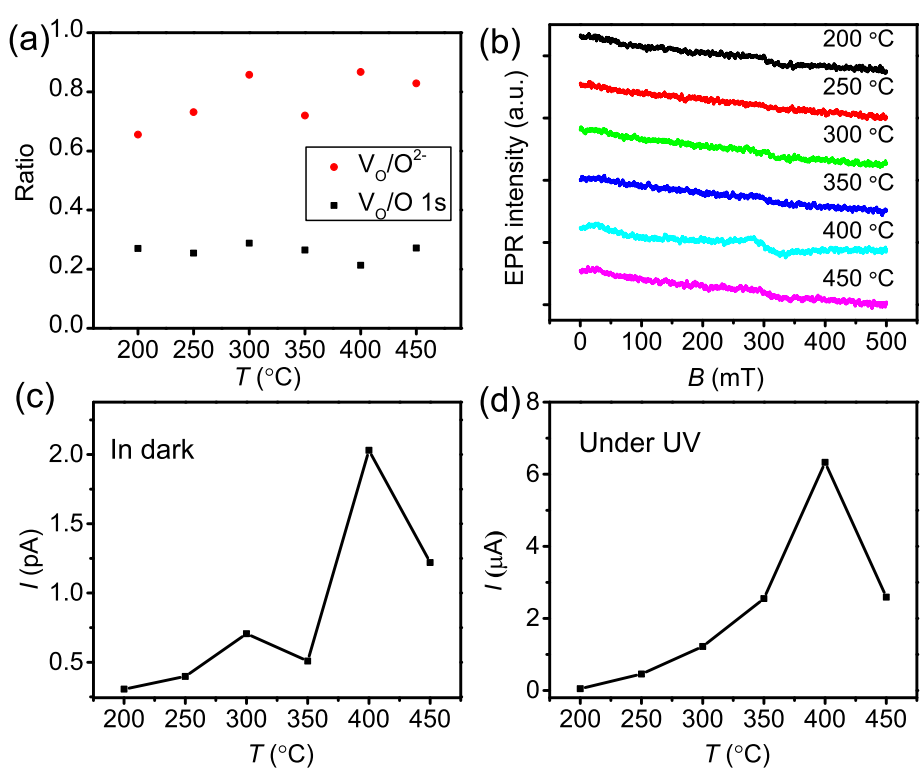

Fig. 2. (Color online) Influence of the annealing temperatures on the V_O concentration, V_O^{1+} concentration, and conductivities. (a) Relationship between the ratio of V_O peak to the O 1s peak and the annealing temperature. (b) EPR spectra of ZnO nanofilms annealed in different temperatures indicate that the relative concentration of the single ionized oxygen vacancy is small and its influence on gas sensing is negligible. (c) Currents of ZnO nanofilms annealed in different temperatures and in the dark. (d) Currents of ZnO nanofilms annealed in different temperatures and under UV light.

defect emissions, PL results have to be analyzed in combination with other methods. The PL spectra of ZnO films annealed in different temperatures are shown in Fig. 3a. The intensity is normalized by the intensity of UV emission [59]. The spectra can be divided into three emission regions: UV emission (Fig. 3b), blue emission (Fig. 3c) and red emission (Fig. 3d). Interestingly, a similar pattern is found in these emission regions. The UV emission shows a red shift (380 to 395 nm, 3.26 to 3.13 eV) with the increase of annealing temperature from 200 to 400 °C, and the shift is reversed (395 to 385 nm, 3.13 to 3.22 eV) with the further increase of the annealing temperature. For the blue/green emission (430–490 nm), the intensity increases with the increase of annealing temperature from 200 to 400 °C, and the trend is reversed with the further increase of annealing temperature. For the orange/red emission (610 to 720 nm), the intensity decreases with the increase of annealing temperature from 200 to 350 °C, and the correlation is reversed with further increase of the annealing temperature (the peak at 600 nm is caused by the 300 nm excitation source used). The annealing temperature around 400 °C is a turning point for all three emission regions.

The UV emission is related with the exciton emission near the band gap. The red shift of UV emission has been observed previously, and is due to the increase of carrier density introduced by oxygen vacancies [40]. In other words, when the annealing temperature increases from 200 to 400 °C, the concentration of V_O^{2+} increases, and further increase of temperature would result to the decrease of V_O^{2+} concentration. As to the blue/green emission (430–490 nm), it is attributed to the defect emission of oxygen vacancy [30,39,57,60–62], transition between V_O^{1+} and photoexcited holes [40,56,63], transition involves V_O^{2+} [64], or surface defects [59]. Since the EPR spectra indicates that the concentration of V_O^{1+} in our sample is negligible, the transition that involves V_O^{1+} can be excluded. As to the orange/red emission, transitions related with interstitial oxygen [65,66], surface defects [67], and oxygen vacancy are proposed [68–70].

To pinpoint the origin of these emissions, the band structures of ZnO and ZnO $(10\bar{1}0)$ surface with V_O in different states are calculated, as shown in Fig. 4. ZnO $(10\bar{1}0)$ surface is used to represent the ZnO surfaces due to its highest surface area in ZnO wurtzite structure and large intensity in XRD spectra (Fig. S2 online). The band gap of perfect ZnO bulk is 3.4 eV and corresponds to the 365 nm UV emission. The neutral oxygen vacancy would result to a defect state 1.62 eV above the valence band, and hence the orange/red emission. V_O^{2+} acts as shallow donor and its state lies 3.13 eV above the valence band. For ZnO $(10\bar{1}0)$ surface, its band gap narrows to 3.14 eV. Consequently, both V_O^{2+} in ZnO bulk and ZnO surface states would result to the decrease of band gap, i.e., the red shift of UV emission in PL spectra. On ZnO $(10\bar{1}0)$ surface, V_O^{2+} would introduce a defect state 2.68 eV above the valence band, and result to the blue emission around 463 nm. Consequently, the

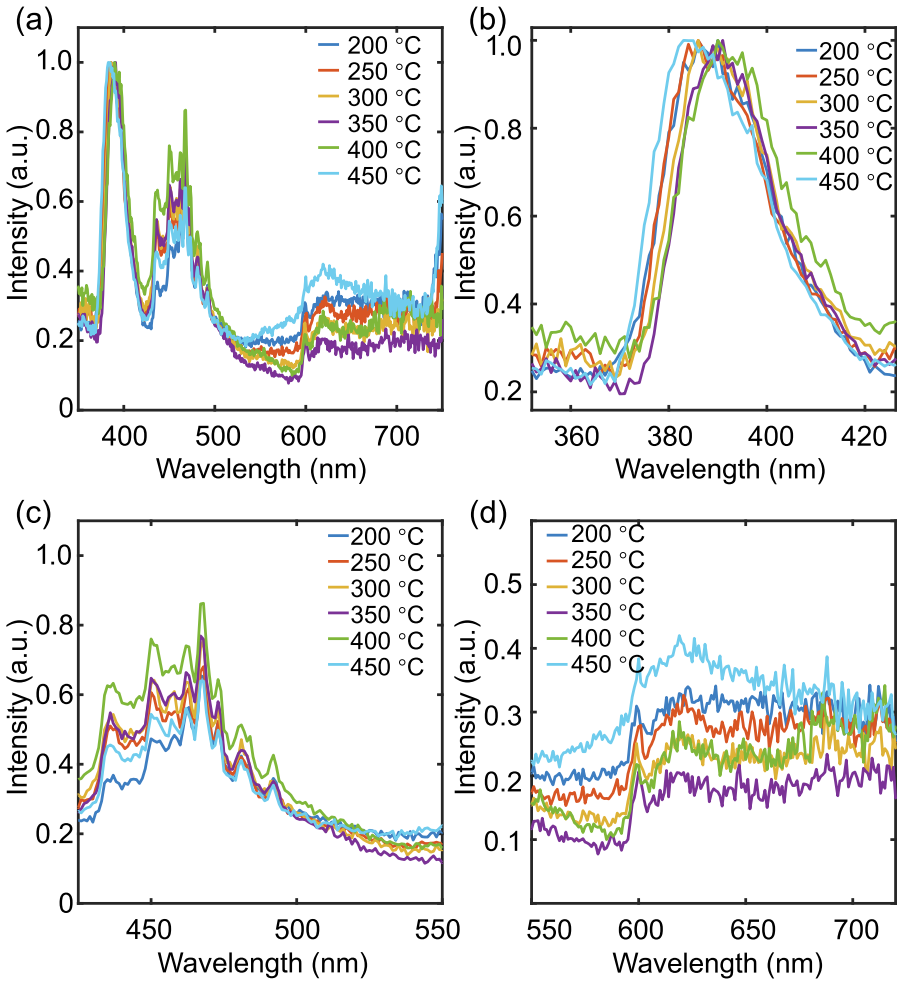

Fig. 3. (Color online) PL spectra of ZnO nanofilms annealed in different temperatures. The spectra are normalized by the intensity of near-band emission. The whole PL spectra of ZnO nanofilms annealed in different temperatures (a) can be divided into three regions: UV emission (b), blue emission (c) and red emission (d).

three emission regions in PL spectra of ZnO are all related with the transition between V_O^0 and V_O^{2+} states. The red shift of UV emission, increase of blue/green emission and decrease of orange/red emission are all corelated with the increase of V_O^{2+} concentration and the decrease of V_O^0 concentration. Taken the difference in formation energy into consideration, the turning point (annealing temperature around 400 °C) can be explained by the transition between V_O^0 and V_O^{2+}. With the increase of annealing temperature, V_O^0 transforms to V_O^{2+} and the density of electrons released from V_O^{2+} increases. The Fermi level would increase correspondingly until it surpasses the thermal transition energy, where the formation energy of V_O^0 becomes smaller than that of V_O^{2+}, and a reverse transition from V_O^{2+} to V_O^0 is resulted. This reverse transition would lead to the blue shift of UV emission, the decrease of blue/green emission and the increase of orange/red emission in PL spectra. This can be further verified by the deconvolution of PL spectra using Gaussian functions (Figs. S5–S8 and Tables S3–S5 online): peaks at 395, 468, 436 and 450–460 nm are attributed to the bulk V_O^{2+}, surface V_O^{2+}, Zn_i, and V_O^{2+}-Zn_i duel defect [17] respectively, and the intensities of these peaks all reach the maximum when annealed at 400 °C (Fig. S8 online).

3.2. Gas sensing performance and mechanism

To understand the influence of V_O states on gas sensing properties, NO_2 gas sensors based on ZnO nanofilms annealed at different temperatures are fabricated and their response to NO_2 gas (mixed with air) are measured, as shown in Fig. 5. The sensor response is defined as the ratio between the resistance change of ZnO nanofilm when exposing to NO_2/air mixed gas ($R_{gas} - R_{air}$) and the resistance of ZnO nanofilm in air (R_{air}). A good linearity is obtained between the response of gas sensors and the concentration of NO_2 (represented by c), as shown in Fig. 5a. Furthermore, in all samples annealed for 120 min, the ZnO nanofilms annealed at 400 °C exhibit the largest response, which reaches 1.54×10^4 to 100 ppm NO_2. The 400 °C annealing temperature once again acts as a turning point for the gas sensing properties of ZnO, which is correlated with the transition between V_O^0 and V_O^{2+}. Compared with the V_O concentration (Fig. 2a), crystallite size of ZnO (Fig. S2 and Table S1 online), lattice strain within (Fig. S3 and Table S2 online) and surface morphology of ZnO (Fig. S4 online), the turning point in the NO_2 responses of ZnO films is not related with all these factors and can only be explained by the transition between V_O^0 and V_O^{2+} during annealing. The response can be further enhanced with the annealing duration adjusted, as shown in Fig. 5b. The response reaches 3.34×10^4 to 100 ppm NO_2. This ultrasensitive response makes it suitable to detect ppb-level NO_2 as shown in Fig. 5c, d. The 165% response to 25 ppb NO_2 is obtained, and the response is quite stable during 5 sensing cycles (the difference in responses is within 7%). Compared with the reported responses of ZnO gas sensors, the ZnO nanofilm gas sensor in this work has the largest response to per ppb NO_2 gas, and do not need to be heated while operating, as shown in Table 1. Furthermore, the responses of ZnO gas sensors are not reduced by the increase of relative humidity, as shown in Fig. S9 (online). A larger UV current is observed when sensing within a higher relative humidity, which is caused by the dissociation of water molecule [71,72] and results to the

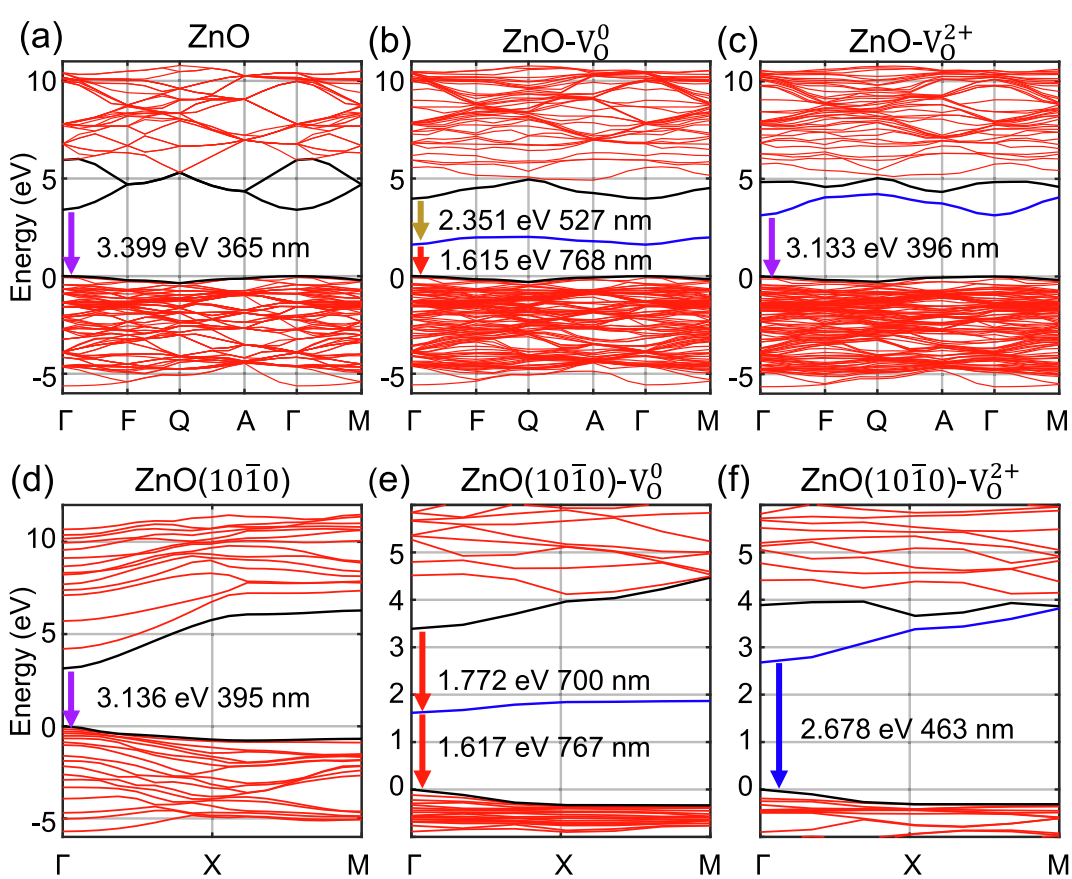

Fig. 4. (Color online) Calculated band structures of ZnO bulk (a–c) and (10$\bar{1}$0) surface (d–f) with oxygen vacancy in different states. The states resulted from vacancy are shown in blue lines, and the conduction/valence bands are shown in black lines. The possible transitions and corresponding wavelength of emissions are indicated by the arrows.

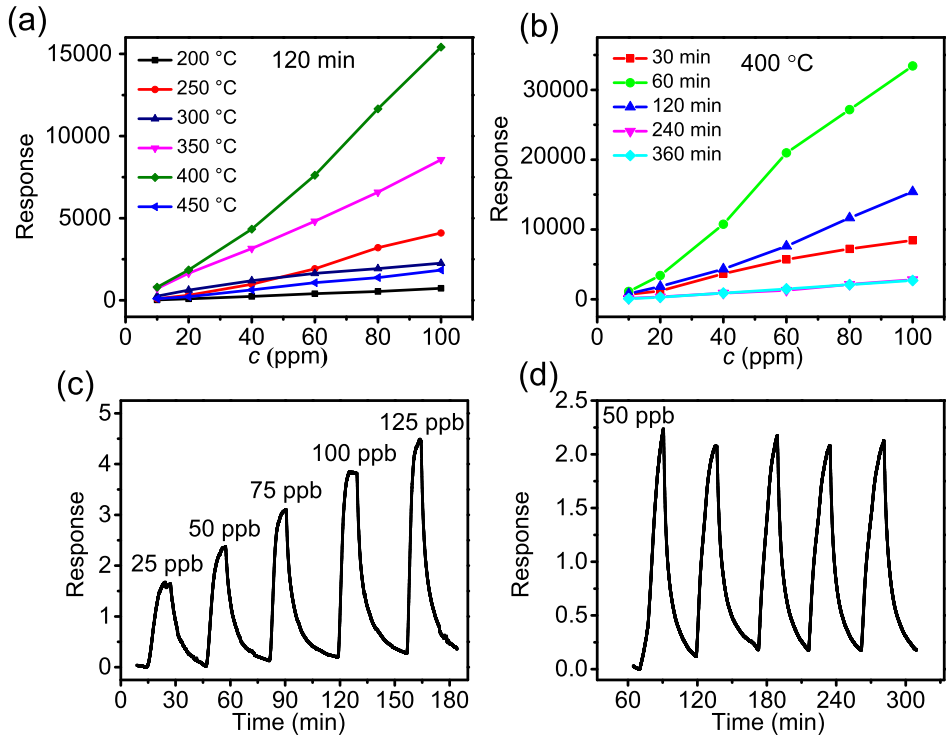

Fig. 5. (Color online) Responses of ZnO nanofilms annealed in different temperatures to different concentrations of NO_2. (a) ZnO annealed in 400 °C exhibits the highest response to NO_2. (b) ZnO annealed in 400 °C and for 60 min exhibits the highest response. (c) The ppb-level NO_2 gas sensing is achieved and 1.65 response to 25 ppb NO_2 is obtained. (d) Good repeatability to 50 ppb NO_2 is demonstrated.

Table 1
Comparison between the responses of this work and the reported ZnO gas sensors. RT represents room temperature.

Materials	Structure	NO_2 concentration	Response	Conditions	Ref.
ZnO	Nanofilms	25 ppb	165%	RT UV light	This work
ZnO	Nanofibers	25 ppb	16%	100 ℃ UV light	[76]
ZnO	Nanowires	100 ppb	102%	300 ℃	[77]
ZnO	Nanoflowers	250 ppb	~10	200 ℃	[78]
p-Si/n-ZnO	Diodes	250 ppb	−9.8%	Solar light	[79]
SnO_2/ZnO	Nanowires	500 ppb	13.4	RT UV light	[80]
ZnO	Nanowires	500 ppb	15	225 ℃	[73]
ZnO	Fibers	770 ppb	18	175 ℃	[81]
ZnO	Nanowire	1 ppm	7.08	RT UV light	[14]
SnO_2/ZnO	Core–shell nanowires	1 ppm	238.73%	RT UV light	[82]
ZnO	Mesoporous sheets	1 ppm	135%	RT	[83]
ZnO	Nanorods	1 ppm	100%	RT	[84]

increase of response to NO_2. It also should be noted that when the NO_2 concentration is quite low (below 100 ppb), the linear relationship between response and NO_2 concentration is no longer satisfied, and the response would decrease quickly, as shown in references [1,73–75].

Up to now, it is proven that during the post annealing treatment, a transition between V_O^0 and V_O^{2+} is involved and a high concentration of V_O^{2+} would result to an ultrasensitive response to NO_2. The adsorbed NO_2 or ambient O_2 would cause the depletion of electrons from ZnO, and oxygen vacancy in ZnO can enhance the adsorption of both species. As discussed in our previous work [34], the equilibrium of adsorption is determined by the interplay between the binding energy of adsorbates, extrinsic surface states of adsorbates, the Fermi level and surface band bending of ZnO. Since the extrinsic surface states of adsorbed O_2 and NO_2 are at a similar level (around 0.35 eV below the conduction band) [34], and intrinsic properties (Fermi level and surface band bending) of ZnO are identical for the adsorption of O_2 and NO_2, the equilibrium of adsorption and the consequential response of ZnO gas sensor to NO_2 would depend on the binding energy of O_2 and NO_2 only. As a result, the binding energy of O_2 and NO_2 on ZnO with oxygen vacancy in different states should be compared. The binding energy can be calculated by the following formula

$$\Delta E_{ads} = (E_{ZnO} + E_{ads}) - E_{ads/ZnO}, \quad (3)$$

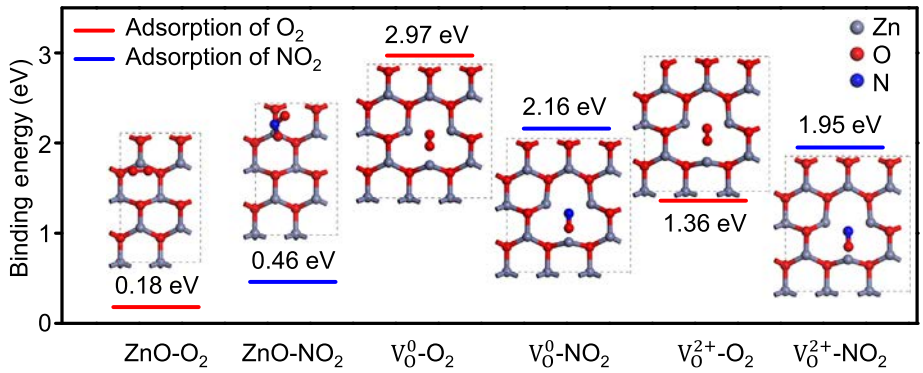

Fig. 6. (Color online) The calculated geometric configurations and corresponding adsorption energies of O_2 and NO_2 on ZnO, ZnO with neutral oxygen vacancy, and doubly ionized oxygen vacancy respectively.

where ΔE_{ads} is the binding energy,E_{ZnO} is the total energy of the ZnO surface, E_{ads} is the total energy of the NO_2 or O_2 molecule, $E_{ads/ZnO}$ is the total energy of the ads/ZnO system (where ads is NO_2 or O_2). Hence, a positive binding energy indicates a favourable adsorption and stable structure.

The results and the corresponding geometric configurations are shown in Fig. 6 (side views of the geometric structures are shown in Fig. S10 online). In the top view of geometric configurations, only first atomic layer of ZnO (1 0 0) surface is shown for clarity. On perfect ZnO (1 0 0) surface, the binding energy of NO_2 (0.46 eV) is larger than that of O_2 (0.18 eV) and the adsorption of NO_2 is favoured. The binding energy of both molecules would increase when oxygen vacancy is introduced. However, adsorption of O_2 is stronger when the oxygen vacancy is neutral due to the larger binding energy (2.97 eV of O_2 compared with 2.16 eV of NO_2). Due to the limited adsorption sites and the large difference in binding energy, the adsorption of O_2 would be quite favoured on V_O^0 and correspondingly V_O^0 cannot promote the adsorption of NO_2 efficiently. When V_O^{2+} is introduced, the binding energy of NO_2 (1.95 eV) becomes larger than that of O_2 (1.36 eV) and the difference in binding energy of NO_2 and O_2 on V_O^{2+} (0.59 eV) is larger than that on perfect ZnO surface (0.28 eV). Consequently, the adsorption of NO_2 on V_O^{2+}would be favoured and the response would be enhanced dramatically. In other words, V_O^{2+} is far more efficient than V_O^0 to enhance the adsorption of NO_2 when ambient O_2 is present and the transition from V_O^0 to V_O^{2+} caused by the post annealing treatment can increase the response to NO_2 of ZnO gas sensor.

Since V_O^0 is neutral and V_O^{2+} releases two free electrons into ZnO, the transition between these two states should lead to a similar influence on the conductivity: the conductivity should increase with the annealing temperature and then decrease after the turning point (around 400 °C). This is exactly what we observed (Fig. 2c, d): the conductivities of ZnO films fabricated under a same condition except for the annealing temperature exhibit a turning point at 400 °C both in dark and under UV light. Due to the surface adsorption of ambient oxygen, ZnO films would be depleted in dark and illumination of UV light with enough intensity can remove this depletion player. So, the conductivity under UV light is related with the concentration of V_O^{2+} and ZnO annealed at 400 °C has the largest concentration of V_O^{2+} and largest conductivity, in accordance with the PL spectra and gas sensing results. Since the binding energy of O_2 on V_O^0 (2.97 eV) is larger than that on V_O^{2+} (1.36 eV), the concentration of carriers depleted by adsorbed O_2 would decrease when oxygen vacancies transform from the neutral to the doubly ionized states. Consequently, when in the dark, the conductivity of ZnO nanofilm also has the largest conductivity when annealed at 400 °C.

4. Conclusion

In conclusion, the influence of V_O states on NO_2 sensing properties of ZnO nanofilm is investigated and the underlying mechanism is clarified in this study. The post annealing process would result to the transformation of V_O from the neutral to the doubly ionized state. The neutral V_O would favor the adsorption of ambient O_2, while the doubly ionized V_O can enhance the adsorption of NO_2 due to the difference in the binding energies of NO_2 and O_2 on V_O in different states. Consequently, the transformation of V_O from the neutral to the doubly ionized state can enhance the response to NO_2 dramatically as a result of the stronger adsorption of NO_2 than the competitive adsorption of ambient O_2. No direct correlation is found between the NO_2 response and the V_O concentration, crystallite size or surface roughness, which indicates that the response enhancement cannot be attributed to the increase of V_O concentration as mostly suggested. Following this mechanism, a dramatic response enhancement of ZnO nanofilm NO_2 gas sensor is achieved, which realizes the ppb-level NO_2 gas sensing (165% response to 25 ppb NO_2) with a good repeatability.

Conflict of interest

The authors declare that they have no conflict of interest.

Acknowledgments

This work was supported by the National Program for Support of Top-notch Young Professionals, the Fundamental Research Funds for the Central Universities (lzujbky-2018-ot04), and the National Natural Science Foundation of China (81702095).

Author contributions

Yong Qin conceived and designed the experiments. Gaoda Li conceived the model and performed the simulation. Heng Zhang performed the experiments. Leixin Meng and Xiaoyu Huang fabricated the materials. Zhao Chen conducted the PL measurements. Zhe Sun conducted the AFM measurements. All authors contributed to the discussions and preparation of manuscript.

Supplementary materials

Supplementary materials to this article can be found online at https://doi.org/10.1016/j.scib.2020.05.027.

References

[1] Li YX, Zu BY, Guo YN, et al. Surface superoxide complex defects-boosted ultrasensitive ppb-level NO_2 gas sensors. Small 2016;12:1420–4.
[2] Yuan H, Aljneibi SAAA, Yuan JR, et al. ZnO nanosheets abundant in oxygen vacancies derived from metal-organic frameworks for ppb-level gas sensing. Adv Mater 2019;31:1807161.
[3] Hancke GP, Silva Bde C, Hancke GP. The role of advanced sensing in smart cities. Sensors 2012;13:393–425.
[4] Ou JZ, Yao CK, Rotbart A, et al. Human intestinal gas measurement systems: *in vitro* fermentation and gas capsules. Trends Biotechnol 2015;33:208–13.
[5] Puckett JL, George SC. Partitioned exhaled nitric oxide to non-invasively assess asthma. Respir Physiol Neurobiol 2008;163:166–77.
[6] Meng LX, Xu Q, Sun Z, et al. Enhancing the performance of room temperature ZnO microwire gas sensor through a combined technology of surface etching and UV illumination. Mater Lett 2018;212:296–8.
[7] Zhang J, Liu XH, Neri G, et al. Nanostructured materials for room-temperature gas sensors. Adv Mater 2016;28:795–831.
[8] Ahn MW, Park KS, Heo JH, et al. Gas sensing properties of defect-controlled ZnO-nanowire gas sensor. Appl Phys Lett 2008;93:263103.
[9] Al-Hardan N, Abdullah MJ, Aziz AA. The gas response enhancement from ZnO film for H_2 gas detection. Appl Surf Sci 2009;255:7794–7.
[10] Al-Hashem M, Akbar S, Morris P. Role of oxygen vacancies in nanostructured metal-oxide gas sensors: a review. Sens Actuators B 2019;301:126845.
[11] Chen M, Wang ZH, Han DM, et al. Porous ZnO polygonal nanoflakes: synthesis, use in high-sensitivity NO_2 gas sensor, and proposed mechanism of gas sensing. J Phys Chem C 2011;115:12763–73.
[12] Fan FY, Feng YJ, Bai SL, et al. Synthesis and gas sensing properties to NO_2 of ZnO nanoparticles. Sens Actuators B 2013;185:377–82.
[13] Park Y, Yoo R, Sr Park, et al. Highly sensitive and selective isoprene sensing performance of ZnO quantum dots for a breath analyzer. Sens Actuators B 2019;290:258–66.
[14] Wang J, Shen Y, Li X, et al. Synergistic effects of UV activation and surface oxygen vacancies on the room-temperature NO_2 gas sensing performance of ZnO nanowires. Sens Actuators B 2019;298:126858.
[15] Yu WW, Shen ZG, Peng F, et al. Improving gas sensing performance by oxygen vacancies in sub-stoichiometric WO_{3-x}. RSC Adv 2019;9:7723–8.
[16] Zhang LX, Yin YY. Large-scale synthesis of flower-like ZnO nanorods via a wet-chemical route and the defect-enhanced ethanol-sensing properties. Sens Actuators B 2013;183:110–6.
[17] Xue ZG, Cheng ZX, Xu J, et al. Controllable evolution of dual defect Zn_i and V_O associate-rich ZnO nanodishes with (0001) exposed facet and its multiple sensitization effect for ethanol detection. ACS Appl Mater Interfaces 2017;9:41559–67.
[18] Wang X, Wang TK, Si GK, et al. Oxygen vacancy defects engineering on Ce-doped α-Fe_2O_3 gas sensor for reducing gases. Sens Actuators B 2020;302:127165.
[19] Zou CW, Liang F, Xue SW. Synthesis and oxygen vacancy related NO_2 gas sensing properties of ZnO:Co nanorods arrays gown by a hydrothermal method. Appl Surf Sci 2015;353:1061–9.
[20] Wang S, Huang D, Xu SS, et al. Two-dimensional NiO nanosheets with enhanced room temperature NO_2 sensing performance via Al doping. Phys Chem Chem Phys 2017;19:19043–9.
[21] Pati S, Banerji P, Majumder SB. Properties of indium doped nanocrystalline ZnO thin films and their enhanced gas sensing performance. RSC Adv 2015;5:61230–8.
[22] Li Z, Yi JX. Enhanced ethanol sensing of Ni-doped SnO_2 hollow spheres synthesized by a one-pot hydrothermal method. Sens Actuators B 2017;243:96–103.
[23] Kim W, Choi M, Yong K. Generation of oxygen vacancies in ZnO nanorods/films and their effects on gas sensing properties. Sens Actuators B 2015;209:989–96.
[24] Xia T, Wallenmeyer P, Anderson A, et al. Hydrogenated black ZnO nanoparticles with enhanced photocatalytic performance. RSC Adv 2014;4:41654–8.
[25] Xia T, Cao YH, Oyler NA, et al. Strong microwave absorption of hydrogenated wide bandgap semiconductor nanoparticles. ACS Appl Mater Interfaces 2015;7:10407–13.
[26] Pan XY, Yang MQ, Fu XZ, et al. Defective TiO_2 with oxygen vacancies: synthesis, properties and photocatalytic applications. Nanoscale 2013;5:3601–14.
[27] Liu J, Gong SP, Quan L, et al. Influences of cooling rate on gas sensitive tin oxide thin films and a model of gradient distributed oxygen vacancies in SnO_2 crystallites. Sens Actuators B 2010;145:657–66.
[28] Liu JQ, Gong SP, Fu QY, et al. Time-dependent oxygen vacancy distribution and gas sensing characteristics of tin oxide gas sensitive thin films. Sens Actuators B 2010;150:330–8.
[29] Zhou XY, Wang AQ, Wang Y, et al. Crystal-defect-dependent gas-sensing mechanism of the single ZnO nanowire sensors. ACS Sens 2018;3:2385–93.
[30] Yu LM, Guo F, Liu S, et al. Both oxygen vacancies defects and porosity facilitated NO_2 gas sensing response in 2D ZnO nanowalls at room temperature. J Alloys Compd 2016;682:352–6.
[31] Elger AK, Baranyai J, Hofmann K, et al. Direct operando spectroscopic observation of oxygen vacancies in working ceria-based gas sensors. ACS Sens 2019;4:1497–501.
[32] Zhang C, Luo YF, Xu JQ, et al. Room temperature conductive type metal oxide semiconductor gas sensors for NO_2 detection. Sens Actuators A 2019;289:118–33.
[33] Yao D, Dong CW, Bing QM, et al. Oxygen-defective ultrathin $BiVO_4$ nanosheets for enhanced gas sensing. ACS Appl Mater Interfaces 2019;11:23495–502.
[34] Li GD, Sun Z, Zhang DY, et al. Mechanism of sensitivity enhancement of a ZnO nanofilm gas sensor by UV light illumination. ACS Sens 2019;4:1577–85.
[35] Lany S, Zunger A. Anion vacancies as a source of persistent photoconductivity in II-VI and chalcopyrite semiconductors. Phys Rev B 2005;72:035215.
[36] Oba F, Togo A, Tanaka I, et al. Defect energetics in ZnO: a hybrid Hartree-Fock density functional study. Phys Rev B 2008;77:245202.
[37] Agoston P, Albe K, Nieminen RM, et al. Intrinsic n-type behavior in transparent conducting oxides: a comparative Hybrid-functional study of In_2O_3, SnO_2, and ZnO. Phys Rev Lett 2009;103:245501.
[38] Li H, Schirra LK, Shim J, et al. Zinc oxide as a model transparent conducting oxide: a theoretical and experimental study of the impact of hydroxylation, vacancies, interstitials, and extrinsic doping on the electronic properties of the polar ZnO (0002) surface. Chem Mater 2012;24:3044–55.
[39] Wei XQ, Man BY, Liu M, et al. Blue luminescent centers and microstructural evaluation by XPS and Raman in ZnO thin films annealed in vacuum, N_2 and O_2. Phys B 2007;388:145–52.
[40] Liu HY, Zeng F, Lin YS, et al. Correlation of oxygen vacancy variations to band gap changes in epitaxial ZnO thin films. Appl Phys Lett 2013;102:181908.
[41] Meyers ST, Anderson JT, Hung CM, et al. Aqueous inorganic inks for low-temperature fabrication of ZnO TFTs. J Am Chem Soc 2008;130:17603–9.
[42] Clark SJ, Segall MD, Pickard CJ, et al. First principles methods using CASTEP. Z Kristallogr 2005;220:567–70.
[43] Payne MC, Teter MP, Allan DC, et al. Iterative minimization techniques for *ab initio* total-energy calculations: molecular dynamics and conjugate gradients. Rev Mod Phys 1992;64:1045–97.
[44] Kohn W, Sham LJ. Self-consistent equations including exchange and correlation effects. Phys Rev 1965;140:A1133–8.
[45] Hohenberg P, Kohn W. Inhomogeneous electron gas. Phys Rev 1964;136:B864–71.
[46] Perdew JP, Ruzsinszky A, Csonka GI, et al. Restoring the density-gradient expansion for exchange in solids and surfaces. Phys Rev Lett 2008;100:136406.
[47] Sheetz RM, Ponomareva I, Richter E, et al. Defect-induced optical absorption in the visible range in ZnO nanowires. Phys Rev B 2009;80:195314.
[48] Laskowski R, Christensen NE. *Ab initio* calculation of excitons in ZnO. Phys Rev B 2006;73:045201.
[49] Li K, Luo YY, Liu B, et al. High-performance NO_2-gas sensing of ultrasmall $ZnFe_2O_4$ nanoparticles based on surface charge transfer. J Mater Chem A 2019;7:5539–51.
[50] Reddy AJ, Kokila MK, Nagabhushana H, et al. Structural, optical and EPR studies on ZnO:Cu nanopowders prepared via low temperature solution combustion synthesis. J Alloys Compd 2011;509:5349–55.
[51] Kaftelen H, Ocakoglu K, Thomann R, et al. EPR and photoluminescence spectroscopy studies on the defect structure of ZnO nanocrystals. Phys Rev B 2012;86:014113.
[52] Evans SM, Giles NC, Halliburton LE, et al. Further characterization of oxygen vacancies and zinc vacancies in electron-irradiated ZnO. J Appl Phys 2008;103:043710.
[53] Wang XJ, Vlasenko LS, Pearton SJ, et al. Oxygen and zinc vacancies in as-grown ZnO single crystals. J Phys D Appl Phys 2009;42:175411.
[54] Bindu P, Thomas S. Estimation of lattice strain in ZnO nanoparticles: X-ray peak profile analysis. J Theor Appl Phys 2014;8:123–34.
[55] Mishra SK, Roy H, Lohar AK, et al. A comparative assessment of crystallite size and lattice strain in differently cast A356 aluminium alloy. IOP Conf Ser: Mater Sci Eng 2015;75:012001.
[56] Sambandam B, Michael RJ, Manoharan PT. Oxygen vacancies and intense luminescence in manganese loaded ZnO microflowers for visible light water splitting. Nanoscale 2015;7:13935–42.
[57] Børseth TM, Svensson BG, Kuznetsov AY, et al. Identification of oxygen and zinc vacancy optical signals in ZnO. Appl Phys Lett 2006;89:262112.
[58] Djurišić AB, Leung YH, Tam KH, et al. Green, yellow, and orange defect emission from ZnO nanostructures: influence of excitation wavelength. Appl Phys Lett 2006;88:103107.
[59] Djurišić AB, Choy WCH, Roy VAL, et al. Photoluminescence and electron paramagnetic resonance of ZnO tetrapod structures. Adv Funct Mater 2004;14:856–64.
[60] Wang QP, Zhang DH, Ma HL, et al. Photoluminescence of ZnO films prepared by r.f. sputtering on different substrates. Appl Surf Sci 2003;220:12–8.
[61] Kang HS, Kang JS, Kim JW, et al. Annealing effect on the property of ultraviolet and green emissions of ZnO thin films. J Appl Phys 2004;95:1246–50.
[62] Tong YH, Liu YC, Lu SX, et al. The optical properties of ZnO nanoparticles capped with polyvinyl butyral. J Sol-Gel Sci Technol 2004;30:157–61.
[63] Vanheusden K, Seager CH, Warren WL, et al. Correlation between photoluminescence and oxygen vacancies in ZnO phosphors. Appl Phys Lett 1996;68:403–5.
[64] van Dijken A, Meulenkamp EA, Vanmaekelbergh D, et al. The kinetics of the radiative and nonradiative processes in nanocrystalline ZnO particles upon photoexcitation. J Phys Chem B 2000;104:1715–23.
[65] Greene LE, Law M, Goldberger J, et al. Low-temperature wafer-scale production of ZnO nanowire arrays. Angew Chem Int Ed 2003;42:3031–4.

[66] Kwok WM, Djurišić AB, Leung YH, et al. Time-resolved photoluminescence study of the stimulated emission in ZnO nanoneedles. Appl Phys Lett 2005;87:093108.
[67] Ong HC, Du GT. The evolution of defect emissions in oxygen-deficient and -surplus ZnO thin films: the implication of different growth modes. J Cryst Growth 2004;265:471–5.
[68] Kumar V, Swart HC, Ntwaeaborwa OM, et al. Origin of the red emission in zinc oxide nanophosphors. Mater Lett 2013;101:57–60.
[69] Studenikin SA, Golego N, Cocivera M. Fabrication of green and orange photoluminescent, undoped ZnO films using spray pyrolysis. J Appl Phys 1998;84:2287–94.
[70] Kong YC, Yu DP, Zhang B, et al. Ultraviolet-emitting ZnO nanowires synthesized by a physical vapor deposition approach. Appl Phys Lett 2001;78:407–9.
[71] Zhang YS, Yu K, Jiang DS, et al. Zinc oxide nanorod and nanowire for humidity sensor. Appl Surf Sci 2005;242:212–7.
[72] Erol A, Okur S, Comba B, et al. Humidity sensing properties of ZnO nanoparticles synthesized by sol–gel process. Sens Actuators B 2010;145:174–80.
[73] Ahn MW, Park KS, Heo JH, et al. On-chip fabrication of ZnO-nanowire gas sensor with high gas sensitivity. Sens Actuators B 2009;138:168–73.
[74] Chen M, Wang ZH, Han DM, et al. High-sensitivity NO_2 gas sensors based on flower-like and tube-like ZnO nanomaterials. Sens Actuators B 2011;157:565–74.
[75] Wu EX, Xie Y, Yuan B, et al. Ultrasensitive and fully reversible NO_2 gas sensing based on p-type $MoTe_2$ under ultraviolet illumination. ACS Sens 2018;3:1719–26.
[76] Aziz A, Tiwale N, Hodge SA, et al. Core-shell electrospun polycrystalline ZnO nanofibers for ultra-sensitive NO_2 gas sensing. ACS Appl Mater Interfaces 2018;10:43817–23.
[77] Park S, An S, Ko H, et al. Synthesis of nanograined ZnO nanowires and their enhanced gas sensing properties. ACS Appl Mater Interfaces 2012;4:3650–6.
[78] Agarwal S, Rai P, Gatell EN, et al. Gas sensing properties of ZnO nanostructures (flowers/rods) synthesized by hydrothermal method. Sens Actuators B 2019;292:24–31.
[79] Hoffmann MW, Mayrhofer L, Casals O, et al. A highly selective and self-powered gas sensor via organic surface functionalization of p-Si/n-ZnO diodes. Adv Mater 2014;26:8017–22.
[80] Lu GY, Xu J, Sun JB, et al. UV-enhanced room temperature NO_2 sensor using ZnO nanorods modified with SnO_2 nanoparticles. Sens Actuators B 2012;162:82–8.
[81] Lee H-U, Ahn K, Lee S-J, et al. ZnO nanobarbed fibers: fabrication, sensing NO_2 gas, and their sensing mechanism. Appl Phys Lett 2011;98:193114.
[82] Park S, An S, Mun Y, et al. UV-enhanced NO_2 gas sensing properties of SnO_2-core/ZnO-shell nanowires at room temperature. ACS Appl Mater Interfaces 2013;5:4285–92.
[83] Chen RS, Wang J, Xiang L. Facile synthesis of mesoporous ZnO sheets assembled by small nanoparticles for enhanced NO_2 sensing performance at room temperature. Sens Actuators B 2018;270:207–15.
[84] Xia Y, Wang J, Li X, et al. Nanoseed-assisted rapid formation of ultrathin ZnO nanorods for efficient room temperature NO_2 detection. Ceram Int 2016;42:15876–80.

Gaoda Li is a Ph.D. candidate of Material Physics and Chemistry under the supervision of Prof. Yong Qin at Lanzhou University and received his B.Sc. degree of Physics at Lanzhou University (2005). From 2017 to 2019, he studied in the group of Prof. Wenzhuo Wu at Purdue University as a joint Ph.D. student. His interests focus on the adsorption process on semiconductor surface, gas sensor, UV sensor as well as applications of density functional theory in the material science.

Heng Zhang is a Master candidate of Material Engineering in the group of Prof. Yong Qin at Lanzhou University and received his B.Sc. degree of Material Physics at Lanzhou University (2018). His current research focuses on the performance improvement of metal oxide semiconductor gas sensors.

Yong Qin received his B.S. degree (1999) in Material Physics and Ph.D. degree (2004) in Material Physics and Chemistry from Lanzhou University. From 2007 to 2009, he worked as a visiting scholar and postdoc in Prof. Zhong Lin Wang's group at Georgia Institute of Technology. Currently, he is a professor at the Institute of Nanoscience and Nanotechnology, Lanzhou University. His research interests include advanced materials, nanoenergy, nanosensor and self-powered nanosystem.